

Non-Equilibrium Relativistic Core Collapse of Self-Interacting Dark Matter Halos – Limits On Seed Black Hole Mass

Hua-Peng Gu,^{1,2} Fangzhou Jiang,^{1,2,*} Xian Chen,^{1,2,†} and Ran Li^{3,4}

¹*Department of Astronomy, School of Physics, Peking University, Beijing 100871, China*

²*Kavli Institute for Astronomy and Astrophysics, Peking University, Beijing 100871, China*

³*School of Physics and Astronomy, Beijing Normal University, Beijing 100875, China*

⁴*School of Astronomy and Space Science, University of Chinese Academy of Sciences, Beijing 100049, China*

(Dated: January 27, 2026)

Recent observations of supermassive black holes (SMBHs) at high redshifts pose challenges to standard seeding mechanisms. Among competing models, the collapse of self-interacting dark matter (SIDM) halos provide a plausible explanation for early SMBH formation. While previous studies on modeling the gravothermal collapse of SIDM halos have primarily focused on non-relativistic evolution under the assumption of hydrostatic equilibrium, we advance this framework by relaxing the equilibrium assumption and additionally incorporating general-relativistic effects. To this end, we introduce the Misner-Sharp formalism to the SIDM context for the first time. Our model reproduces the standard hydrostatic models in the early long-mean-free-path (LMFP) regime, but displays interesting distinct behavior in the late short-mean-free-path (SMFP) regime, where intense outward heat flux drives a rapid expansion of the outer envelope, removing mass from the core and significantly decelerating the collapse. Our general relativistic treatment enables us to follow halo evolution to the final stage when the apparent horizon forms. Our simulation yields a seed black hole mass of approximately 3×10^{-8} of the halo mass at horizon formation, suggesting that additional mechanisms such as baryonic effects are critical for seeding black holes that are sufficiently massive to account for SMBHs in the early Universe.

I. INTRODUCTION

The observation of high-redshift, luminous quasars has revealed the existence of supermassive black holes (SMBHs) in the early universe [1–3]. Traditionally, these black holes (BHs) are thought to originate from stellar-mass seeds—remnants of the first massive stars [4], which grow through continuous accretion [5–7] or mergers [8, 9]. However, the James Webb Space Telescope (JWST) [10] challenged this “light-seed” paradigm by revealing a population of massive compact objects known as the “little red dots” (LRDs) [11] which have been interpreted by many studies as actively accreting SMBHs [12–14]. The LRDs appear unexpectedly abundant at redshifts $4 < z < 9$ and are believed to host BHs with masses ranging from 10^7 to $10^9 M_\odot$ [15, 16]. However, their stellar masses are surprisingly low relative to the scaling relations observed in local active galactic nuclei (AGNs) [17–19]. Reaching such masses by these redshifts requires a seed BH mass of $\gtrsim 10^4 M_\odot$ and uninterrupted Eddington accretion. Consequently, such discovery indicates a significant tension in the standard seeding mechanism, suggesting that light-seed scenarios are insufficient to explain the abundance of high-redshift SMBHs [20].

To explain the origin of high-redshift SMBHs, various baryonic mechanisms have been proposed, including population III remnants, gas-dynamical processes, and stellar-dynamical processes. Population III remnants, however, typically yield seeds of only $\sim 10^2 - 10^3 M_\odot$ [21–23], insufficient to become a promising candidate. More massive seeds may arise from gas-dynamical processes, where the primordial gas cloud could directly collapse into a compact, massive

object under specific conditions, without fragmentation and the subsequent formation of individual stars [24, 25]. Such BH seeds, also named as the direct-collapse BHs (DCBHs), can exceed $10^4 M_\odot$ [24, 26, 27]. Yet, this channel requires the suppression of H_2 cooling via intense UV flux to prevent fragmentation, a condition difficult to achieve without the formation of first-generation stars [28, 29]. Alternatively, stellar-dynamical processes in dense clusters can produce $10^2 - 10^4 M_\odot$ seeds via run-away collisions [30, 31]. However, this mechanism demands extreme stellar densities ($\gtrsim 10^7 M_\odot/\text{pc}^3$) and low metallicity environments that rarely exist simultaneously [32, 33].

Beyond heavy seeds, mechanisms accelerating BH growth, such as super-Eddington accretion [34, 35] and mergers [7, 9, 36], have been explored. While these can theoretically form SMBHs rapidly from light seeds, they face significant environmental constraints. Sustained super-Eddington accretion requires rare, high-density, low-velocity gas reservoirs [37], while mergers are limited by gravitational-wave recoil kicks, which often eject BHs from their fuel sources [7, 38, 39]. Moreover, some cosmological origins, including various types of primordial BHs [22, 40–42] are also considered, where large density fluctuations in the early universe may decouple from the cosmic expansion and collapse into BHs [43–45]. However, to serve as heavy seeds ($> 10^5 M_\odot$), primordial BHs must form near the electroweak decoupling epoch ($t \sim 1$ s), which may risk disturbing Big Bang nucleosynthesis predictions [7, 46]. While the theoretical possibility exists [42, 47], the lack of observation renders the scenario overcomplex and requiring further observations to verify.

Meanwhile, significant progress has been made in dark matter (DM) research. Extensive astronomical observations [48, 49] have established Cold Dark Matter (CDM) as the prevailing paradigm. In this model, DM behaves as a collisionless fluid interacting exclusively via gravity [50, 51], forming

* Corresponding author: fangzhou.jiang@pku.edu.cn

† Corresponding author: xian.chen@pku.edu.cn

large-scale structures and virialized halos [52–55]. However, lacking radiative cooling or thermal conduction due to the collisionless nature, CDM halos cannot collapse further to form BHs [54, 56–58]. Despite its success on large scales, the CDM paradigm faces challenges in matching some small-scale observations [59]. Even by considering baryonic processes that modify CDM halos, the structural diversity of dwarf galaxies cannot be fully accommodated (see e.g., a review by Sales *et al.* [60] and references therein).

This motivates alternative models that modify the collisionless nature of dark matter. The elastic self-interacting DM (SIDM) provides a particularly promising candidate [61]. By introducing a finite self-interaction cross section σ [62, 63], the SIDM model provides viable solutions to most of the small-scale discrepancies while preserving the large-scale success of CDM [61, 64–69]. This is achieved because self-interactions thermalize the central halo, creating the necessary structural diversity—where profiles can be cored or cuspy depending on the cross-section as well as the formation time of the halo—to match observations. According to current observations, the cross section per unit particle mass is constrained to [70, 71] $\sigma \sim 1 - 100 \text{ cm}^2/\text{g}$, with possible velocity dependence that makes the cross section decrease sharply beyond a relative velocity of $\sim 100 \text{ km/s}$ [63]. By heat conduction from the inner core to the outer region [61], these collisions eventually lead to a run-away gravothermal core collapse that occurs within several hundred relaxation timescales [72, 73]. At high redshifts, the core-collapse timescale in high-concentration and early-forming halos can be shorter or comparable to the age of the Universe [74]. Hence, this mechanism offers a plausible pathway for the formation of high-redshift SMBHs [75].

The gravothermal collapse of SIDM halos has been extensively studied in a variety of previous works. Such a process has been modeled using a fluid approximation, where the halo is treated as a spherically symmetric, non-relativistic ideal fluid that undergoes quasi-static collapse under the assumption of hydrostatic equilibrium. This formalism was originally introduced for the study of globular star clusters [76, 77], and was first applied to SIDM halos by Balberg *et al.* [72]. Since then, many studies have addressed the core-collapse time and the density-profile evolution using the fluid model, including the presence of baryonic components [78, 79], partially ultrastrong interactions [33, 80], dissipative interactions [81–85], and velocity-dependent cross sections [86–88]. Complementing the fluid approach, N -body simulations have also been conducted [65, 89–93], although they face significant computational challenges in resolving the core collapse at late times [94, 95].

However, none of these previous studies have been able to determine the final seed BH mass—a parameter essential for assessing the viability of SIDM core-collapse as a high-redshift SMBH seeding mechanism. The limitations of the fluid approximation stem from two fundamental shortcomings: (1) the lack of incorporation of general relativity (GR), and (2) the reliance on the unrealistic assumption of hydrostatic equilibrium. In the Newtonian framework, late-stage evolution leads to a “gravothermal catastrophe,” where central density and temperature diverge [72, 77]. However, this

formalism breaks down as the system inevitably reaches the relativistic limit. In contrast, GR describes this dynamical evolution in a completely different way, where the metric tensor evolves and eventually develops a singularity signaling the formation of the horizon [96, 97]. This necessitates a relativistic framework to determine the final BH mass. Furthermore, the inclusion of GR alone is insufficient because the assumption of hydrostatic equilibrium breaks down during late-stage evolution. As the core contracts, the system’s adiabatic index rises substantially. Applying the general stability criterion derived in Feng *et al.* [98], the core would eventually violate this threshold, triggering a dynamical instability. This transition from quasi-static evolution to rapid gravitational collapse occurs before horizon formation, rendering the hydrostatic approximation invalid. Therefore, currently there exist only estimations of the seed BH mass, based on extrapolation [88] or energy conservation [99]. To rigorously determine this mass, a complete time-dependent GR analysis tracing the non-equilibrium evolution towards horizon formation is required.

Incorporating GR into the non-equilibrium evolution will introduce profound physical consequences that were previously overlooked. As matter falls deep into the relativistic potential well near the horizon, a substantial amount of gravitational energy—comparable to the rest mass energy—is released. In the case of elastic SIDM collisions, which lack radiative dissipation, this energy is converted into kinetic energy and effectively conducted outward as heat. This intense outward heat flux drastically increases the pressure in the outer layers, acting against the collapse. Consequently, this mechanism raises critical questions about the efficiency of subsequent accretion and whether a massive seed BH can indeed form. However, this dynamic effect is entirely missed in previous studies due to the strict enforcement of hydrostatic equilibrium. For example, existing general relativistic treatments [e.g., 100, 101] have often been restricted to static equilibrium solutions, thereby neglecting the consequences of dynamical gravitational energy release. Thus, resolving the true evolutionary trajectory requires capturing this interplay between relativistic collapse and the opposing thermal pressure, which is only possible through a fully non-equilibrium approach.

Calculating the non-equilibrium collapse of a spherically symmetric system is a well-established issue in GR. This calculation can be traced back to Oppenheimer and Snyder [102]. In their work, the collapse of a system composed of pressureless dust with uniform density is semi-analytically calculated. Furthermore, incorporating the pressure, as expressed through the equation of state (EoS), Misner and Sharp [103] derived the Misner-Sharp equations, which were widely employed in calculations about primordial BHs [42] and compact object collapse [104–107]. Notably, the Misner-Sharp equations provide an ideal tool for our purposes, as they encompass both GR effects and dynamical evolution beyond equilibrium. In this work, we apply this formalism to modeling SIDM halo collapse for the first time. However, since the standard equations are adiabatic, we must incorporate heat conduction to adapt the framework for our analysis. We achieve this by introducing a heat flux term into the energy-momentum tensor. This extended general relativistic framework enables us

to trace the full evolutionary history of the halo—from the initial virialized state to the formation of the BH apparent horizon—providing a self-consistent solution to the SMBH seeding problem.

The paper is organized as follows. We begin in Sec. II by reviewing the traditional fluid approximation before introducing our general relativistic formalism based on the Misner-Sharp equations. In Sec. III, we present the full numerical evolution of the SIDM halo, tracing the trajectory from the quasi-static LMFP core expansion phase, through the dynamic SMFP collapse, to the final formation of the BH horizon. Section IV addresses the implications of these results for the SMBH seeding problem, discussing the potential mechanisms that can affect the final mass. Finally, a summary is provided in Sec. V.

II. METHODS

In this section, we introduce the theoretical framework employed to model the evolutionary trajectory of collapsing SIDM halos. We begin by reviewing the traditional fluid approximation before introducing our extended general relativistic formalism based on the Misner-Sharp equations. Throughout this work, we adopt natural units where $c = G = 1$.

A. Traditional fluid method

Under the standard fluid approximation and the assumption of hydrostatic equilibrium, the gravothermal evolution of an SIDM halo is governed by the following set of equations (1) - (4) [72]:

$$\frac{\partial M}{\partial r} = 4\pi r^2 \rho, \quad (1)$$

$$\frac{\partial P}{\partial r} = -\frac{M\rho}{r^2}, \quad (2)$$

$$\frac{L}{4\pi r^2} = -\kappa \frac{\partial T}{\partial r}, \quad (3)$$

$$\frac{\partial L}{\partial r} = -4\pi r^2 \rho \left\{ \left(\frac{\partial}{\partial t} \right)_M \frac{3v^2}{2} + P \left(\frac{\partial}{\partial t} \right)_M \frac{1}{\rho} \right\}. \quad (4)$$

Here, the system is characterized by the matter density $\rho(r, t)$, enclosed mass $M(r, t)$, pressure $P(r, t)$, temperature $T(r, t)$, velocity dispersion $v(r, t)$, and luminosity $L(r, t)$. These equations correspond to mass conservation (1), hydrostatic equilibrium (2), thermal conduction (3), and energy conservation (4), respectively. In thermal equilibrium, the temperature is given by $kT = mv^2$ and the EoS is

$$P = \rho v^2. \quad (5)$$

The conductivity κ in Eq.(3) exhibits different behaviors based on the ratio of the mean free path $\lambda = 1/(\rho\sigma)$ to

the scale height that corresponds to the local dynamical time $H = \sqrt{v^2/(4\pi\rho)}$. In the short mean free path (SMFP) regime, where $\lambda \ll H$, the conductivity follows the standard form $\kappa_{\text{SMFP}} = (3/2)b\rho\lambda^2/(amt_0)$. Here, the constants are $a = \sqrt{16/\pi}$ and $b = 25\sqrt{\pi}/32$ [108], while $t_0 = \lambda/(av)$ is the relaxation time. Conversely, in the long mean free path (LMFP) regime ($\lambda \gg H$), heat transport is described by $\kappa_{\text{LMFP}} = (3/2)C\rho H^2/(mt_0)$ [77], where C serves as a calibration parameter. Following Koda and Shapiro [89], we adopt $C = 0.75$, a value that enables the fluid evolution to match N -body simulation results. To smoothly interpolate between these two limits, the effective conductivity is constructed as $\kappa^{-1} = \kappa_{\text{SMFP}}^{-1} + \kappa_{\text{LMFP}}^{-1}$ [72]. In the LMFP regime, heat flux is directly proportional to the collision rate, so that $\kappa \propto \sigma$; while in the SMFP regime, where frequent collisions hinder transport, $\kappa \propto \sigma^{-1}$.

B. Misner-Sharp formalism

To capture the full non-equilibrium dynamics and general relativistic effects, we must extend the static framework to include bulk motion and spacetime curvature. Following Misner and Sharp [103], we adopt a time-dependent, spherically symmetric metric in the general form:

$$ds^2 = -e^{2\phi(r,t)} dt^2 + e^{\lambda(r,t)} dr^2 + R(r,t)^2 d\Omega^2, \quad (6)$$

where $R(r, t)$ represents the circumferential radius. We adopt a Lagrangian (comoving) coordinate system where the radial coordinate r labels specific fluid shells. In this frame, the fluid 4-velocity simplifies to $u^\mu = (e^{-\phi}, 0, 0, 0)$. It is convenient to utilize the enclosed rest mass A as the radial coordinate. Since the rest mass enclosed within a comoving shell is conserved¹, A is a strictly monotonically increasing function of r :

$$A(r) = 4\pi \int_0^r \rho e^{\lambda/2} R^2 dr, \quad (7)$$

where ρ is the rest mass density. By defining the radial coordinate directly as the rest mass (i.e., choosing $r = A$), the metric component e^λ is constrained by the rest mass conservation:

$$e^{-\lambda/2} = 4\pi R^2 \rho. \quad (8)$$

Consequently, the metric in mass coordinates becomes:

$$ds^2 = -e^{2\phi(A,t)} dt^2 + e^{\lambda(A,t)} dA^2 + R(A,t)^2 d\Omega^2. \quad (9)$$

To describe the gravothermal evolution of the SIDM halo, we extend the perfect fluid energy-momentum tensor to including a heat flux term:

$$T^{\mu\nu} = (\rho' + P)u^\mu u^\nu + Pg^{\mu\nu} + q^\mu u^\nu + q^\nu u^\mu, \quad (10)$$

¹ In SIDM model, if the collision between DM particles is sufficient, then mass shell crossing is avoided.

where $\rho' = (1 + \epsilon)\rho$ is the total energy density, ϵ is the specific internal energy, P is the pressure, and q^μ represents the heat flux 4-vector. We adopt Eckart's formulation for relativistic thermodynamics, where the purely conductive heat transfer is given by [109, 110]:

$$q^\mu = -\kappa h^{\mu\nu} (\nabla_\nu T + T a_\nu), \quad (11)$$

with the projection tensor $h^{\mu\nu} \equiv g^{\mu\nu} + u^\mu u^\nu$ and 4-acceleration $a_\nu \equiv u^\alpha \nabla_\alpha u_\nu$. The orthogonality condition $q^\mu u_\mu = 0$, combined with spherical symmetry, implies that $q^t = 0$ and the angular components vanish. Thus, only the radial component q^r remains non-zero, taking the specific form [101]:

$$q^r = -\kappa e^{-\lambda/2} e^{-\phi} \frac{\partial}{\partial r} (T e^\phi). \quad (12)$$

We further introduce the following fundamental quantities defined in the Misner-Sharp formalism.

The Misner-Sharp mass, representing the total mass-energy enclosed within shell A :

$$m(A, t) \equiv 4\pi \int_0^A \rho (1 + \epsilon) R^2 (\partial R / \partial A) dA. \quad (13)$$

The generalized Lorentz factor:

$$\Gamma \equiv e^{-\lambda/2} \frac{\partial R}{\partial A}. \quad (14)$$

The coordinate velocity, describing the bulk radial motion:

$$U \equiv e^{-\phi} \frac{\partial R}{\partial t}. \quad (15)$$

Finally, the specific enthalpy:

$$w \equiv 1 + \epsilon + \frac{P}{\rho}. \quad (16)$$

By substituting the metric and energy-momentum tensor into the Einstein field equations and the conservation laws ($\nabla_\mu T^{\mu\nu} = 0$), we derive the complete set of hydrodynamic evolution equations [103, 111]:

$$\frac{\partial m}{\partial A} = (1 + \epsilon)\Gamma + \frac{U q}{\rho}, \quad (17)$$

$$\Gamma = \left(1 + U^2 - \frac{2m}{R}\right)^{1/2}, \quad (18)$$

$$\frac{\partial \phi}{\partial A} = -\frac{1}{w} \left[\frac{1}{\rho} \frac{\partial P}{\partial A} + e^{-\phi} \frac{\partial}{\partial t} \left(\frac{q}{4\pi R^2 \rho^2} \right) \right], \quad (19)$$

$$\rho = \frac{\Gamma}{4\pi R^2 (\partial R / \partial A)}, \quad (20)$$

$$\frac{\partial \epsilon}{\partial t} = -P \frac{\partial}{\partial t} \left(\frac{1}{\rho} \right) - e^{-\phi} \frac{\partial}{\partial A} \left(4\pi R^2 q e^{2\phi} \right), \quad (21)$$

$$\frac{\partial U}{\partial t} = -e^{-\phi} \Gamma^2 \frac{\partial \phi}{\partial A} \left(\frac{\partial R}{\partial A} \right)^{-1} + \frac{m}{R^2} + 4\pi P R. \quad (22)$$

To close the system, we adopt an ideal gas EoS:

$$P = (\gamma - 1)\epsilon\rho, \quad (23)$$

where γ is the adiabatic index. For the non-relativistic case, $\gamma = 5/3$, recovering the standard relation Eq. (5) via $\epsilon = \frac{3}{2}kT$. Furthermore, by expressing temperature in terms of specific internal energy ϵ and utilizing Eq. (8) to eliminate λ , the heat flux equation (12) can be rewritten in mass coordinates as²:

$$q = -(\gamma - 1)\kappa e^{-\phi} (4\pi R^2 \rho) \frac{\partial}{\partial A} (e^\phi \epsilon). \quad (24)$$

Equations (15) - (24) constitute the generalized Misner-Sharp formalism, extended here to include the heat conduction term q . This system allows us to solve for the time evolution of the ten dynamical quantities ($R, U, m, \rho, P, \epsilon, w, \Gamma, \phi$, and q) given appropriate initial and boundary conditions. Notably, Eq. (22) serves as the acceleration equation, replacing the hydrostatic equilibrium condition (2). By transforming Eq. (22) back to the spatial coordinate r and taking the adiabatic limit ($q = 0$), we recover the generalization of the TOV equation [112, 113] to the non-static case:

$$e^{-\phi} \frac{\partial U}{\partial t} = \Gamma e^{-\lambda/2} \frac{\partial \phi}{\partial r} - \frac{m + 4\pi R^3 P}{R^2}. \quad (25)$$

This form explicitly demonstrates how the bulk acceleration $\partial U / \partial t$ is driven by the competition between the pressure gradient (first term) and the effective gravity (second term, which includes relativistic corrections). Equation (21) represents energy conservation, replacing Eq. (4), while Eq. (24) serves as the relativistic heat conduction law, replacing Eq. (3).

C. Horizon formation

A critical phenomenon in the gravitational collapse of compact objects is the emergence of horizons. To investigate this, we analyze the behavior of outgoing radial null geodesics during the collapse. Based on the metric in Eq. (9), the derivative operator along such a geodesic is defined as [114]:

$$D_k \equiv e^{-\phi} \frac{\partial}{\partial t} + e^{-\lambda/2} \frac{\partial}{\partial A}. \quad (26)$$

It follows immediately that $D_k A = e^{-\lambda/2} > 0$. This indicates that the rest mass coordinate A increases along the null geodesic, implying that the light ray propagates outward relative to the local matter fluid. However, this does not guarantee that the photon physically expands to larger radial distances.

² The additional factor $4\pi R^2 \rho$ arises from the coordinate transformation $\partial A / \partial r = 4\pi R^2 \rho$. Note that the scalar quantity q appearing in Eqs. (17), (19), and (21) actually represents q^A , therefore leading to the factor $4\pi R^2 \rho$

If the matter collapses rapidly enough, these light rays may be trapped. To quantify this, we combine the definition of Γ in Eq. (14) with the Misner-Sharp equations (15) and (18), yielding the evolution of the areal radius along the ray:

$$D_k R = \frac{1 - 2mR^{-1}}{\Gamma - U}. \quad (27)$$

For any event (t, A) satisfying the condition $R(t, A) < 2m(t, A)$, then it can be deduced that $D_k R(t, A) < 0$, since Γ remains positive in this framework, and for infalling matter $U < 0$. Consequently, light emitted from such a region is dragged inward and cannot escape to infinity. The condition $R(t, A) = 2m(t, A)$ then defines a trapped surface, also named as the apparent horizon, within which even outgoing null geodesics are confined [96]. In contrast, defining the event horizon requires knowledge of the global causal structure of spacetime. During gravitational collapse, the apparent horizon, if it exists at a given time slice, must lie within or coincide with the event horizon [115]. In summary, this Misner-Sharp formalism provides a self-consistent method to precisely calculate the seed BH mass at the moment of apparent horizon formation in the SIDM halo collapse scenario.

D. Numerical setup & method validation

Using the Misner-Sharp formalism, we can numerically solve for the evolution of SIDM halos. We initialize the system using a Navarro-Frenk-White (NFW) density profile [116, 117]:

$$\rho(R, t = 0) = \frac{\rho_s}{(R/R_s)(1 + R/R_s)^2}. \quad (28)$$

We adopt typical halo parameters $R_s = 2.6$ kpc and $\rho_s = 0.019 M_\odot/\text{pc}^3$ [118], corresponding to a halo mass of $M(< 10R_s) = 6.3 \times 10^9 M_\odot$. With a cross-section of $\sigma = 5 \text{ cm}^2/\text{g}$, the characteristic relaxation timescale, defined at the scale radius $R = R_s$, is $t_0 = 0.26$ Gyr. To facilitate the relativistic analysis, we employ natural units and normalize all physical quantities by the total halo mass M . These parameters constitute our fiducial model for the subsequent analysis.

The numerical solution is performed using a Lagrangian discretization scheme based on the mass coordinate A . The system is partitioned into concentric spherical shells, where each shell is labeled by a fixed enclosed rest mass A . Unlike Eulerian grids, the mass coordinate A remains constant for each shell, while its radius $R(A, t)$, bulk velocity $U(A, t)$, and thermodynamic variables (e.g., $\epsilon(A, t)$) evolve dynamically. For the boundary conditions, at the center ($A = 0$), we impose the regularity conditions $R = 0$, $U = 0$, $m = 0$, and $\Gamma = 1$ [107]. At the outer boundary ($A = A_{\text{total}}$), we set $e^\phi = 1$ ³. With these initial and boundary conditions, we numerically solve the coupled system of Eqs. (15) - (24) using

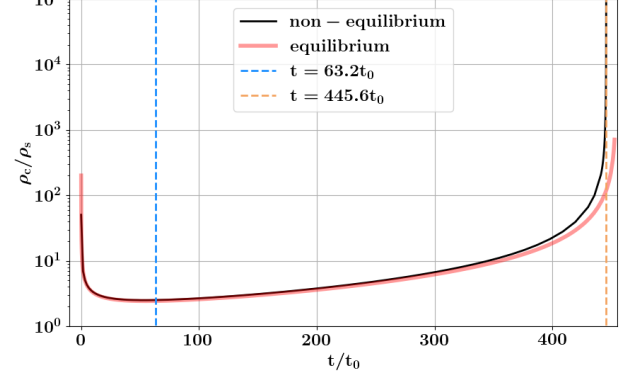


FIG. 1. The evolution of the central density with time, comparing the traditional method (assuming hydrostatic equilibrium, red line) with our proposed method (non-equilibrium, black line). Our non-equilibrium treatment agrees well with the equilibrium fluid model during core formation and the early stages of core collapse, but predicts faster collapse in the late stages.

a finite-difference algorithm. Further details on the numerical implementation are provided in Appendix A.

To validate our formalism and quantify the impact of non-equilibrium effects, we performed a parallel calculation using the traditional hydrostatic method governed by Eqs. (1) - (4), assuming the same initial conditions. Figure 1 compares the central density evolution derived from both approaches. The excellent agreement observed in the early stage confirms the validity of our method in this quasi-static regime. However, as the system evolves, significant deviations appear. In the late stages, the high central density generates a massive heat flux that drives the system away from equilibrium, causing the quasi-static approximation to break down. In this phase, our framework reveals a faster collapse. Physically, this acceleration occurs because the bulk velocity accumulates dynamically via the acceleration equation (22), whereas the traditional method artificially resets this bulk motion to zero at each time step to enforce hydrostatic equilibrium. Employing our non-equilibrium formalism is essential to correctly describe the late-time evolutionary stage and to precisely calculate the final BH mass.

III. RESULTS – Evolution towards BH formation

In this section, we present the complete evolutionary trajectory of the SIDM halo, tracing the pathway from an initial NFW profile to the eventual formation of a BH. This continuous process naturally decomposes into three stages corresponding to distinct dynamical regimes. First, in Sec. III A,

³ This implies that we adopt the proper time of a comoving observer at the outer boundary as our coordinate time. Theoretically, the NFW profile ex-

tends to infinity; however, for numerical feasibility, we truncate the domain at $R = 20R_s$ ($A_{\text{total}} = 1.405M$). Since the halo matter continues beyond this radius, the pressure at the truncation boundary is non-zero, rather than a vacuum condition.

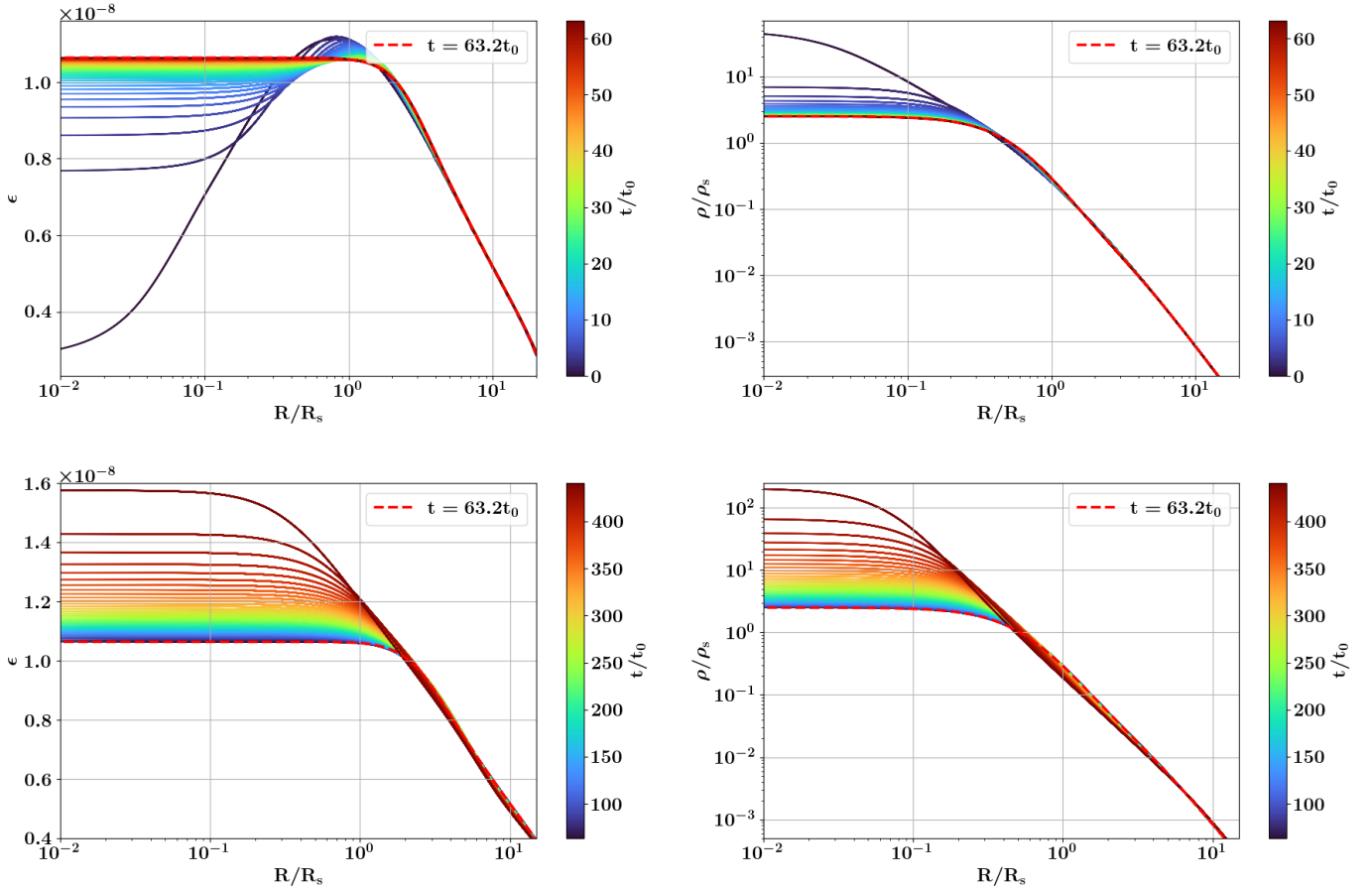


FIG. 2. Evolution of the specific internal energy (left column) and density profiles (right column) for the fiducial halo. The upper panels illustrate the core expansion phase, where the halo evolves from an initial NFW profile ($t = 0$) towards an isothermal core. The lower panels depict the subsequent gravothermal collapse phase. The red dashed line at $t = 63.2t_0$ marks the formation of the isothermal core, serving as the transition boundary between the expansion and collapse regimes. The color gradient of the solid lines represents the progression of time. Note that ϵ denotes the specific internal energy normalized by c^2

we examine the early gravothermal evolution, tracing the core expansion and self-similar collapse in the LMFP regime. Next, in Sec. III B, we investigate the SMFP phase, where outward heat flux and non-equilibrium effects significantly reshape the core structure. Finally, in Sec. III C, we track the terminal relativistic collapse leading to the formation of the BH horizon.

A. Gravothermal evolution

The first stage of SIDM halo evolution is core expansion, a phase extensively discussed in previous literature [119–122]. The upper panels of Figure 2 illustrate the evolutionary trajectories of the specific internal energy and density profiles in this stage, calculated using our Misner-Sharp formalism. Initially, the NFW halo configuration is in hydrostatic equilibrium at all radii, resulting in zero bulk velocity throughout the system. However, heat conduction due to SIDM collisions

redistributes the specific internal energy, modifying the pressure gradient. Consequently, the pressure force no longer balances gravity, inducing bulk motion. Given the temperature profile of an NFW halo, heat is initially transported primarily from radius $R \sim R_s$ toward the center. This process heats the central region, transforming the initial density cusp into an expanding isothermal core. Eventually, a strictly isothermal core forms at the center by $t = 63.2t_0$. It is important to note, however, that the physical expansion phase concludes earlier, at $t = 51.3t_0$ when the central density reaches its minimum. Subsequently, the core density begins to rise as the energy loss from outward heat transfer exceeds the gain from inward flow. By $t = 63.2t_0$, the inward heat flux vanishes entirely, leaving only outward flux, which marks the definitive entry into the gravothermal collapse phase. At the moment of maximum expansion, the central density is $\rho(t = 51.3t_0, A = 0) = 2.5\rho_s$.

The evolution of the specific internal energy and density during the subsequent gravothermal collapse stage is shown in the lower panels of Figure 2. In this phase, heat is transferred

from the core region ($R \gtrsim R_s$) to the outer halo, causing the core to contract. As the core shrinks and its density increases, the heat flux intensifies, accelerating the collapse. For moderate central densities ($\lesssim 10^2 \rho_s$), the LMFP condition $\lambda \gg H$ holds globally, leading to a self-similar evolution [72]⁴. This self-similar collapse persists until $t \approx 445t_0$, when the LMFP condition breaks down in the core region. Before this time, the bulk velocity U is negligible compared to the velocity dispersion v ⁵.

B. SMFP evolution

In our fiducial model, non-equilibrium effects become dominant once the core enters the SMFP regime, corresponding to central densities $\rho_c \gtrsim 10^5 \rho_s$. The evolution of the bulk velocity profile during this stage is presented in the upper panel of Figure 3. The system exhibits a distinct bifurcation into two dynamic regions: a collapsing inner core and a rapidly expanding outer envelope. The interface between these regions propagates inward, indicating that the core is simultaneously shrinking in radius and losing mass due to outflow. This strong mass outflow is driven by the intense heat flux emerging from the high-density core, where thermal conduction is highly efficient. This energy is absorbed by the shells surrounding the core, triggering a rapid expansion with velocities reaching a significant fraction of the velocity dispersion. The resulting density evolution, shown in the lower panel of Figure 3, reveals that this rapid expansion creates a significant density gap just outside the core. Consequently, non-equilibrium dynamics fundamentally alter the density profile during the SMFP phase.

A critical parameter in SMFP evolution is the enclosed mass within the SMFP regime (M_{SMFP}), as it provides the fundamental mass budget for the seed BH. Previous estimates generally posit that a small fraction of M_{SMFP} eventually collapses into the central BH [72, 88, 99, 118, 123]. The boundary of the SMFP regime is indicated by the black-edged dots in the lower panel of Figure 3. To clearly show the evolution of the SMFP mass, we present the trajectory of the SMFP mass fraction in Figure 4, indicated by the black line. The transition begins at $t = 445.0t_0$, when the central density rises sufficiently to satisfy the $\lambda = H$ condition. Subsequently, M_{SMFP} grows, reaching a maximum of approximately $5 \times 10^7 M_\odot$ (1% of the total halo mass) at $t = 445.6t_0$. Following the peak at $t = 445.6t_0$, the SMFP mass begins to decline. This reversal occurs because the core continuously loses mass to outflow, while the surrounding material—already depleted by the aforementioned density gap—is too diffuse to effectively replenish the SMFP region. Shortly thereafter, by $t \approx 445.8t_0$,

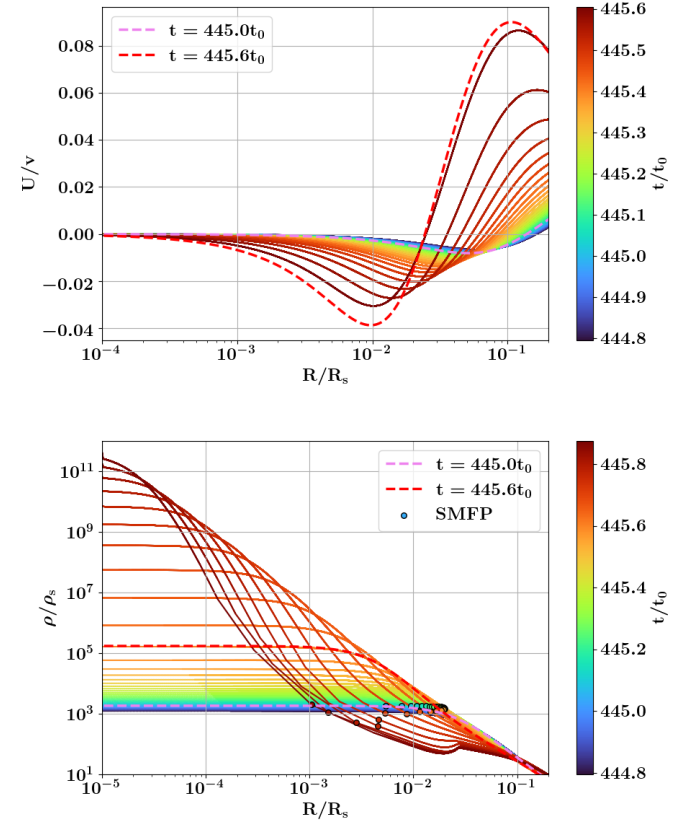


FIG. 3. The evolution of the bulk velocity profile (upper panel) and the density profile (lower panel) during the SMFP core collapse stage. The notations follow those in Figure 2. In the upper panel, the y-axis represents the ratio of the bulk velocity U to the velocity dispersion v , which serves as a diagnostic for deviations from hydrostatic equilibrium. The black-edged dots mark the boundary of the SMFP regime at each evolutionary snapshot. The density depletion in the outer region arises from mass outflow, which is induced by the intense outward heat flux characteristic of the SMFP regime.

the density profile exterior to the core stabilizes⁶, and a dense core with $\rho > 10^{10} \rho_s$ forms within the region $R < 10^{-3} R_s$. The SMFP mass declines to $\sim 10^{-4}$ of the total halo mass at $t = 445.8t_0$ and gradually plateaus afterwards, reflecting the stabilization of the outer halo.

Non-equilibrium effects play a pivotal role here, as they substantially alter the density profile. Our calculated maximum SMFP mass is slightly lower than that reported by Nishikawa *et al.* [118]. This discrepancy arises because our non-equilibrium framework accounts for dynamical accumulation of outflow velocity due to continuous heat conduction, whereas quasi-static approaches determine the outflow rate

⁴ Strictly speaking, self-similarity assumes a quasi-static evolution. In our formalism, which includes bulk velocity, the evolution approximates self-similarity in the LMFP regime because the bulk velocity remains much smaller than the velocity dispersion.

⁵ In our relativistic formalism, we utilize specific internal energy ϵ rather than v . These quantities are related via $v^2 = (\gamma - 1)\epsilon$.

⁶ Stability here refers to the density profile shape; it does not imply that mass outflow has ceased. Mass outflow persists, but since the remaining core mass is negligible compared to the total mass of the outer shells, further outflow does not significantly perturb the outer density structure.

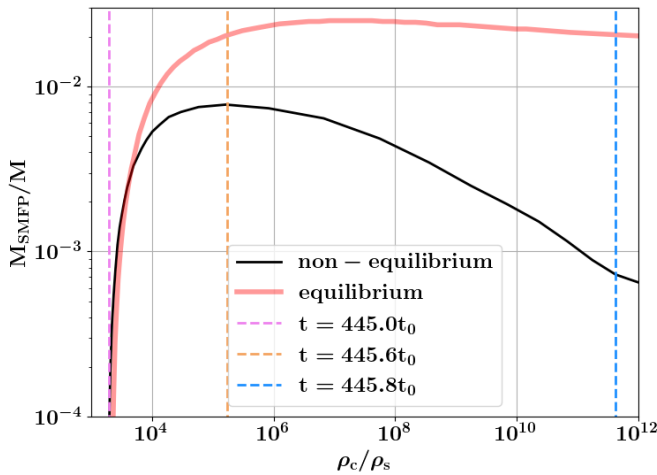


FIG. 4. Evolution of the SMFP mass fraction with central density, comparing the traditional method (assuming hydrostatic equilibrium, red line) with our proposed method (non-equilibrium, black line). In the non-equilibrium case, the SMFP regime emerges at $t = 445.0t_0$, reaches its maximum enclosed mass at $t = 445.6t_0$, and gradually stabilizes after $t = 445.8t_0$. In contrast, the equilibrium calculation yields a substantially larger SMFP mass.

solely based on the instantaneous thermal state. To quantify this deviation, we plot the hydrostatic result in Figure 4 (red line) for comparison. In the hydrostatic case, the SMFP mass fraction peaks at $\sim 2.5\%$ and nearly stabilizes at this value in the subsequent evolution. This implies that the unrealistic assumption of the hydrostatic equilibrium would overestimate the SMFP mass, which is critical for determining the final BH mass.

C. Black hole formation

By the end of SMFP evolution, although the central density of the SMFP core eventually exceeds $\rho > 10^{10}\rho_s$, the compactness m/R within the core grows only to $\sim 10^{-6}$ in natural units, remaining far from the BH formation threshold. In the late-time evolution, the core mass decreases due to continuous mass outflow, yet the core radius shrinks at a faster rate, leading to an increase in the ratio m/R over time. Our general relativistic formalism enables us to track the evolution continuously until the horizon formation ($R = 2m$), thereby allowing us to directly calculate the seed BH mass at formation, which has never been exactly realized in previous studies.

To visualize the system's approach towards horizon formation, we present the evolution of the mass-radius ($m - R$) relation in Figure 5. Within these profiles, the core radius R_{core} corresponds to the prominent turning point, marking the boundary of the collapsing core. In the non-relativistic regime (upper panel, where $m_{\text{core}}/R_{\text{core}} \ll 1$), the collapse exhibits self-similar behavior again. While both the core mass and radius decrease continuously, the shape of the mass pro-

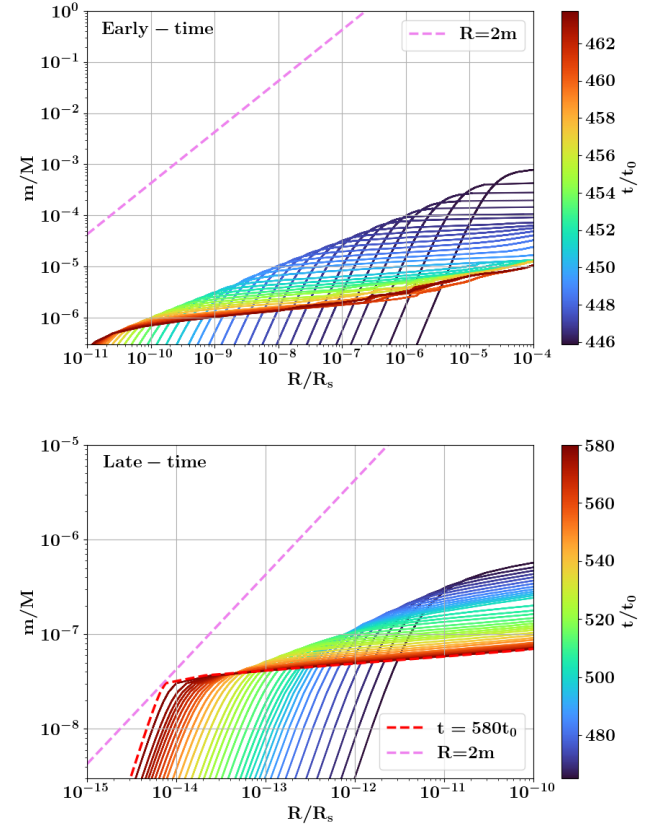


FIG. 5. The evolution of the mass profile at BH formation stage. The upper panel traces the $m - R$ evolution in the non-relativistic regime ($m_{\text{core}}/R_{\text{core}} \lesssim 10^{-2}$), while the lower panel displays the strong-gravity regime approaching the horizon ($m_{\text{core}}/R_{\text{core}} \gtrsim 10^{-2}$). The violet dashed lines represent the apparent horizon condition $R = 2m$. At $t = 580t_0$, the mass profile (red dashed line) intersects $R = 2m$, marking the formation of the central BH. Other notations follow those in Figure 2. The seed BH mass at horizon formation is about 3×10^{-8} of the halo mass ($\approx 200 M_{\odot}$).

file remains invariant. The envelope of the mass profiles approximates a power-law relation $m_{\text{core}} \propto R_{\text{core}}^{1/2}$, indicating an increase in compactness over time. It is important to note that, despite introducing bulk velocity into our formalism, the core's evolution in this regime can still be approximated as quasi-static. This is because the bulk velocity in the deep core remains negligible compared to the local sound speed. According to the acceleration equation (22), when the core shrinks to extremely small scales ($R_{\text{core}} \sim 10^{-10}R_s$), any slight deviation from hydrostatic equilibrium induces a massive acceleration via the pressure gradient, which immediately restores the system to its equilibrium state. Consequently, non-equilibrium effects are significant only in the rapidly expanding outer envelope, which have negligible impact on the central core dynamics. Leveraging this physical property, we adopt a quasi-static approximation while retaining GR effects for the central region during this phase to accelerate numerical

calculation⁷.

Notably, Figure 5 reveals a counter-intuitive feature: the collapse rate of the core decreases over time, as evidenced by the extended duration required for the system to bridge the final orders of magnitude between m and R . Such deceleration happens at $t \approx 445.8t_0$ due to rapid expansion of the surrounding shells, which stands in contrast to the standard expectation of a run-away collapse process [72]. However, this phenomenon is physically consistent within our framework: the intense outward heat flux significantly increases the pressure in the outer layers, effectively impeding further collapse. We can verify this deceleration quantitatively by estimating the collapse timescale. In this late stage, the core evolution is governed by the conductive heat loss. Therefore, the characteristic collapse time can be estimated via

$$t_c = \frac{E_{\text{core}}}{4\pi R_{\text{core}}^2 q_{\text{core}}}, \quad (29)$$

where E_{core} is the total internal energy of the core, and q_{core} is the heat flux at the core boundary. At $t = 445.8t_0$, when the core enters the self-similar collapse phase, we find $t_c \sim 0.1t_0$, signifying a rapid collapse. However, during the self-similar evolution, the core shrinks significantly, causing the total heat luminosity $4\pi R_{\text{core}}^2 q_{\text{core}}$ to decrease. This reduction in energy loss rate progressively lengthens the collapse timescale t_c . By $t \approx 460t_0$, the timescale increases to $t_c \sim 40t_0$, indicating that the collapse has become significantly slower.

As the compactness parameter grows toward the strong gravity regime ($2m/R \rightarrow 1$), the evolutionary trajectory begins to deviate from the self-similar solution, as illustrated in the lower panel of Figure 5. During this phase, although the quasi-static approximation remains valid for the core, the general relativistic terms in Eq. (22) significantly modify the hydrostatic equilibrium structure. The Γ^2 factor associated with the pressure term reduces the effective pressure support as $\Gamma \rightarrow 0$ when $2m/R \rightarrow 1$, leading to a denser core. Consequently, the evolutionary track deviates from the $m_{\text{core}} \propto R_{\text{core}}^{1/2}$ scaling, exhibiting a noticeably shallower gradient in the logarithmic plot. This deviation implies a more rapid convergence toward $R = 2m$ condition. When the central temperature rises sufficiently such that the velocity dispersion becomes comparable to the speed of light, the dynamical instability is triggered [98], leading to a rapid dynamical collapse. Finally, at $t = 580t_0$, the mass profile intersects the horizon condition $R = 2m$ at $m \approx 3 \times 10^{-8}M$. This event marks the formation of a central black hole with a mass of $M_{\text{BH}} \approx 200 M_{\odot}$.

IV. DISCUSSION

Our numerical simulations for the fiducial model, governed by the general relativistic Misner-Sharp formalism, indicate that the SIDM halo ultimately collapses to form a BH of $M_{\text{BH}} \approx 200 M_{\odot}$ at $t = 580t_0$. Notably, our results align with the recent estimates of Gad-Nasr *et al.* [88] and Feng *et al.* [99], which derived the seed mass based on SMFP evolution via self-similar extrapolation and energy conservation arguments, respectively. By providing the first fully relativistic calculation of this BH formation process, we confirmed that some earlier works [72, 89, 118, 123] have overestimated the seed mass. Crucially, our complete evolutionary history uncovers the physical origin of this discrepancy: previous studies underestimated the non-equilibrium effects, where intense outward heat flux from the core can effectively hinder the gravitational collapse.

Nevertheless, the resulting seed BH mass is significantly below the threshold ($\gtrsim 10^4 M_{\odot}$) typically required to explain the progenitors of observed high-redshift SMBHs. This suggests that the pure SIDM collapse scenario, under standard halo parameters, may face difficulties in directly producing sufficiently heavy seeds. Hence, in this section, we investigate the dependence of the seed BH mass on halo parameters and explore additional physical mechanisms—specifically the inclusion of baryons, post-formation accretion, or the velocity-dependent cross-section—that could be incorporated into our framework to enhance the seed mass.

The relatively low mass of the seed BH is primarily a consequence of the prolonged mass outflow phase identified in Section III B. As the core enters the SMFP regime, efficient outward heat conduction drives a significant portion of the core mass into the expanding envelope. Throughout this evolution, the core maintains a self-similar scaling relation of approximately $m_{\text{core}} \propto R_{\text{core}}^{1/2}$. This power-law dependence implies that the final seed mass is intrinsically coupled to the halo's initial structural parameters; specifically, the initial compactness M/R_s sets the baseline for this evolutionary trajectory, with higher compactness halos naturally yielding more massive seeds. Furthermore, the self-interaction cross-section σ plays a critical role during the LMFP-SMFP transition. Since the thermal conductivity in the SMFP regime scales as $\kappa \propto \sigma^{-1}$, a larger σ reduces the efficiency of heat conduction. This suppression of outward heat flux mitigates mass loss, allowing the SMFP core to retain a larger fraction of its mass and effectively elevating the normalization of the $m_{\text{core}} - R_{\text{core}}$ relation. To quantitatively investigate the dependence of the seed BH mass on these parameters, we performed two additional simulations with different parameter sets, evolving the system from the initial NFW profile to the formation of the SMFP core. The results are shown in Table I, where we also list the maximum SMFP mass in these simulations as they serve as the fundamental mass budget for the seed BH.

A critical factor omitted in this DM-only simulation is the presence of baryons. In a realistic protogalactic halo, baryons would fall into the deep gravitational potential well created by the collapsing SIDM core. Unlike dark matter, baryons can undergo dissipative cooling via radiative processes, allowing

⁷ In principle, the time step is strictly limited by the sound speed via the Courant-Friedrichs-Lowy condition (Eq. (A12), see Appendix A). However, since the system's evolution is governed by the bulk velocity, virtually no physical evolution occurs within such a constrained time step, leading to extreme computational inefficiency. By adopting the quasi-static assumption, the instability associated with the sound speed is suppressed, allowing us to safely adopt a much larger time step.

TABLE I. Dependence of the seed BH mass on model parameters. The columns list the halo mass, the characteristic radius of the initial NFW profile, the self-interaction cross-section, the maximum SMFP mass, and the final BH mass^a.

$M (M_\odot)$	R_s (kpc)	σ (cm ² /g)	Max $M_{\text{SMFP}} (M_\odot)$	$M_{\text{BH}} (M_\odot)$
6.3×10^9	2.6	5	5×10^7	200
6.3×10^9	0.65	5	1.7×10^8	700
6.3×10^9	2.6	20	1.2×10^8	500

^a The latter two simulations were terminated upon the formation of the maximum SMFP core. Consequently, their final BH masses are estimated based on the self-similar scaling relation.

them to condense more efficiently than the conductive SIDM fluid. The high-density SIDM core calculated in our work ($\rho > 10^{10} \rho_s$) would serve as an ideal gravitational trap for such infalling gas. Previous studies have demonstrated that the dynamical interplay between SIDM gravothermal collapse and baryonic components can significantly accelerate the collapse rate [78, 79, 90, 91, 124]. Consequently, it is reasonable to infer that the resulting BH mass would increase correspondingly due to the deepened gravitational potential.

Furthermore, a BH seed of baryonic origin, such as a Population III stellar remnant, may form at the halo center prior to the completion of the SIDM collapse. Although such a seed might be initially low-mass, its presence would fundamentally alter the system's evolution. In our current SIDM-only simulations, the BH emerges only at the very final stage; prior to this, despite extreme densities, the core mass remains insufficient to trigger horizon formation, and the dynamics are dominated by mass outflow. However, the existence of a pre-existing central BH imposes an absorptive inner boundary condition. This would effectively circumvent the mass outflow phase: matter infalling toward the center would be accreted onto the BH rather than accumulating pressure to drive an outward flow. Since mass accretion across the horizon is irreversible—matter cannot be “pushed back” once accreted—this mechanism would prevent mass loss and facilitate rapid BH growth. We intend to incorporate these baryonic physics and central accretion dynamics in our future work.

It is important to emphasize that $M_{\text{BH}} \approx 200 M_\odot$ represents only the initial mass at the instant of horizon formation. Although our simulations indicate that at the time of horizon formation, accretion is inhibited by a steep pressure gradient driven by outward heat flux, this suppression may be temporary. Once the horizon forms, the core is trapped and the outward heat flux is causally cut off, potentially removing the thermal barrier and allowing the infall of outer shells to resume. Moreover, recent studies propose that the presence of baryons could further facilitate this accretion process [99], potentially leading to a much larger final mass. In the presence of baryons, a higher fraction of the halo mass may enter the SMFP regime, thereby offering a more substantial reservoir for seed BH accretion.

Based on our simulation results, we perform a simplified estimation of the potential growth of the seed BH via Bondi accretion [125, 126]. At the instant of horizon formation, the

typical sound speed in the outer regions is $c_s \sim 2000 \text{ km/s}$, yielding a Bondi radius of $R_B = 2GM_{\text{BH}}/c_s^2 \sim 1.5 \times 10^{-10} R_s$. The enclosed mass within this radius is merely $\sim 10^{-7}$ of the total halo mass ($\approx 600 M_\odot$). Although this instantaneous reservoir is small, the critical factor is the continuous inflow of material from the outer shells. Assuming steady-state accretion, the Bondi rate is [99] $\dot{M}_{\text{B}} = 4\pi\lambda_s G^2 M_{\text{BH}}^2 \rho c_s^{-3} \sim 10^8 M_\odot/\text{Gyr}$, where $\lambda_s = 0.25$ and we evaluate ρ and c_s at R_B . However, given the steep radial decline of the density profile, such an extreme accretion rate is unsustainable. To rigorously quantify the cumulative mass growth of the BH seed, it requires future extended simulations using our Misner-Sharp formalism.

Distinct from accretion dynamics, a velocity-dependent cross-section could also fundamentally alter the late-time evolution. As investigated by previous works [e.g., 63], the cross-section σ is expected to be as high as $\sigma \gtrsim 100 \text{ cm}^2/\text{g}$ at low velocities but suppressed at $v \gtrsim 10^3 \text{ km/s}$. If this model were incorporated into our simulation, the high cross-section in the low-velocity outer halo would significantly shorten the relaxation time, accelerating the initial core formation. In our fiducial model, the BH formation time $580t_0$ exceeds the cosmic age; thus, introducing a velocity-dependent cross-section may be essential⁸. However, in the late stages as the core temperature rises, σ would drop significantly. One possibility is that the core transitions into the LMFP regime where the collision rate becomes insufficient to sustain heat conduction, potentially causing the collapse to stall. Alternatively, if the core remains in the SMFP regime, the reduced cross-section would actually enhance thermal conductivity since $\kappa \propto \sigma^{-1}$, leading to a vastly different collapse trajectory. Resolving which of these competing mechanisms dominates requires future simulations incorporating velocity-dependent interactions.

V. CONCLUSION

In this work, we have developed a fully general relativistic and hydrodynamical framework based on the Misner-Sharp formalism to investigate the gravothermal collapse of SIDM halos. Unlike previous quasi-static approaches, our method explicitly captures non-equilibrium dynamic effects, enabling us to track the system's evolution continuously from the initial core expansion phase to the formation of an apparent horizon.

Our numerical results demonstrate consistency with traditional quasi-static approaches during the early evolutionary stages, verifying the validity of our formalism. However, as the system becomes denser, our simulations reveal that the late-stage dynamics in the SMFP regime are dominated by intense outward heat flux. This thermal transport drives a substantial mass outflow, decelerating the collapse and depleting the core mass significantly before the BH forms. For a representative halo with $M \sim 10^9 M_\odot$ and constant cross-section

⁸ Alternatively, a higher halo concentration could also reduce the relaxation timescale t_0

$\sigma = 5 \text{ cm}^2/\text{g}$, the maximum SMFP mass is about 1% of the halo mass and the resulting seed BH mass is approximately 200 M_\odot —corresponding to a seed-to-halo mass ratio of $\approx 3 \times 10^{-8}$. We also investigated their dependence on halo parameters and the cross-section of the SIDM.

This result suggests that pure SIDM gravothermal collapse with constant cross-section faces challenges in directly producing the heavy seeds required for high-redshift SMBHs. To reconcile this discrepancy, we propose that additional physical mechanisms are essential. Specifically, the inclusion of baryons—which facilitate accretion by deepening the potential—as well as the consideration of post-horizon evolution and velocity-dependent cross-section, is critical for enhancing the seed mass. Future extensions of our formalism incorporating these effects will be necessary to fully constrain the role of SIDM in SMBH formation.

The code used to model SIDM halo evolution in the Misner-Sharp framework is publicly available at <https://github.com/Hua-Peng-G/SIDM>.

ACKNOWLEDGMENTS

We thank Wei-Xiang Feng for helpful discussions. This work was supported by the National Key Research and Development Program of China (Grant No.2024YFC2207300) and the National Natural Science Foundation of China (Grant No. 12473037). FJ acknowledges support by the National Natural Science Foundation of China (NSFC, 12473007) and China Manned Space Program with grant no. CMS-CSST-2025-A03. RL acknowledges the support of National Nature Science Foundation of China (No 11988101), the science research grants from the China Manned Space Program (No. CMS-CSST-2025-A0), CAS Project for Young Scientists in Basic Research (No. YSBR-062).

Appendix A: Numerical Implementation

We employ a finite-difference algorithm with a staggered Lagrangian grid to numerically solve the system of Eqs. (15) - (24). We denote the temporal step by the superscript n ($n = 0, 1, \dots$) and the spatial grid index by the subscript i . The spatial domain is discretized into N mass shells, with grid interfaces defined by the enclosed mass $\{A_i\}_{i=0}^N$.

In this staggered grid scheme, variables are defined either at the cell interfaces or at the cell centers:

- Interface variables (defined at i): radius R , bulk velocity U , Lorentz factor Γ , Misner-Sharp mass m , lapse function e^ϕ , and heat flux q .
- Cell-centered variables (defined at $i - 1/2$): Rest mass density ρ , specific internal energy ϵ , pressure P , and specific enthalpy w .

The discretization proceeds sequentially as follows. Note that for variables defined at cell centers, values at the interface i

are approximated via arithmetic averaging, e.g., $\bar{P}_i \equiv (P_{i-1/2} + P_{i+1/2})/2$.

1. Update Velocity (U): Using variables from the previous time step $n - 1$:

$$U_i^n = U_i^{n-1} + \Delta t \left[(\Gamma_i^{n-1})^2 \left(\frac{\partial \phi}{\partial A} \right)_i^{n-1} \times (4\pi(R_i^{n-1})^2 \bar{\rho}_i^{n-1}) - (e^\phi)_i^{n-1} \left(\frac{m_i^{n-1}}{(R_i^{n-1})^2} + 4\pi R_i^{n-1} \bar{P}_i^{n-1} \right) \right], \quad (\text{A1})$$

where the potential gradient term is given by:

$$\left(\frac{\partial \phi}{\partial A} \right)_i^{n-1} = \frac{-1}{2\bar{w}_i^{n-1}} \left[\frac{P_{i+1/2}^{n-1} - P_{i-1/2}^{n-1}}{\bar{\rho}_i^{n-1} (A_{i+1/2} - A_{i-1/2})} + \frac{\sigma}{(e^\phi)_i^{n-1} \Delta t} \left(\frac{q_i^{n-1}}{4\pi(R_i^{n-1})^2 (\bar{\rho}_i^{n-1})^2} - \frac{q_i^{n-2}}{4\pi(R_i^{n-2})^2 (\bar{\rho}_i^{n-2})^2} \right) \right]. \quad (\text{A2})$$

2. Update Radius (R):

$$R_i^n = R_i^{n-1} + (e^\phi)_i^{n-1} U_i^n \Delta t. \quad (\text{A3})$$

3. Update Lorentz Factor (Γ): We utilize m_i^{n-1} as an approximation for m_i^n to decouple the implicit dependence⁹:

$$\Gamma_i^n = \sqrt{1 + (U_i^n)^2 - \frac{2m_i^{n-1}}{R_i^n}}. \quad (\text{A4})$$

4. Update Density (ρ):

$$\rho_{i-1/2}^n = \frac{(A_i - A_{i-1})(\Gamma_{i-1}^n + \Gamma_i^n)/2}{\frac{4\pi}{3} [(R_i^n)^3 - (R_{i-1}^n)^3]}. \quad (\text{A5})$$

5. Update Internal Energy (ϵ):

$$\epsilon_{i-1/2}^n = \epsilon_{i-1/2}^{n-1} - P_{i-1/2}^{n-1} \left(\frac{1}{\rho_{i-1/2}^n} - \frac{1}{\rho_{i-1/2}^{n-1}} \right) - \frac{4\pi \Delta t}{e^\phi_{i-1/2}^n} \left[\frac{\mathcal{F}_i^{n-1} - \mathcal{F}_{i-1}^{n-1}}{A_i - A_{i-1}} \right], \quad (\text{A6})$$

where $\mathcal{F}_i \equiv (R_i)^2 q_i (e_i^\phi)^2$.

6. Update Pressure (P) and Enthalpy (w):

$$P_{i-1/2}^n = (\gamma - 1) \rho_{i-1/2}^n \epsilon_{i-1/2}^n, \quad (\text{A7})$$

$$w_{i-1/2}^n = 1 + \epsilon_{i-1/2}^n + \frac{P_{i-1/2}^n}{\rho_{i-1/2}^n}. \quad (\text{A8})$$

⁹ Strictly, Γ^n depends on m^n . However, calculating m^n requires Γ^n . For sufficiently small time steps, using m^{n-1} provides a valid first-order approximation.

7. Update Metric Potential (ϕ): Integrated inward from the boundary condition $(e^\phi)_N^n = 1$:

$$\ln((e^\phi)_i^n) = \ln((e^\phi)_{i+1}^n) - \frac{1}{2}(A_{i+1} - A_i) \left[\left(\frac{\partial \phi}{\partial A} \right)_i^n + \left(\frac{\partial \phi}{\partial A} \right)_{i+1}^n \right]. \quad (\text{A9})$$

8. Update Heat Flux (q):

$$q_i^n = -\frac{3}{2}(\gamma - 1)^{3/2}a \times \left(\frac{1}{C} + \frac{a \sigma^2}{b 4\pi} \bar{P}_i^n \right)^{-1} \times \frac{\sqrt{\bar{\epsilon}_i^n} \cdot \bar{P}_i^n \cdot (R_i^n)^2 \cdot 2 \left[(e^\phi)_{i+1/2}^n - (e^\phi)_{i-1/2}^n \right]}{(e^\phi)_i^n \cdot \bar{\rho}_i^{-1} \cdot (A_{i+1} - A_{i-1})}, \quad (\text{A10})$$

where $\bar{\rho}^{-1}$ denotes the average of the inverse density.

9. Update Misner-Sharp Mass (m):

$$m_i^n = m_{i-1}^n + (A_i - A_{i-1}) \left[\bar{\Gamma}_i^n (1 + \epsilon_{i-1/2}^{n-1}) + \frac{(U_{i-1}^n + U_i^n)(q_{i-1}^n + q_i^n)}{4\rho_{i-1/2}^{n-1}} \right], \quad (\text{A11})$$

with the boundary condition $m_0^n = 0$.

The numerical time step Δt is strictly constrained by the Courant-Friedrichs-Lowy (CFL) condition [127]:

$$\Delta t \lesssim \min_i \left(\frac{\Delta R_i}{|U_i| + c_{s,i}} \right), \quad (\text{A12})$$

where $c_{s,i} = \sqrt{P_i/\rho_i}$ denotes the local sound speed. Typically, the bulk velocity U remains much smaller than c_s . However,

in the SMFP regime, particularly in regions of rapid expansion (as shown in Figure 4), the bulk velocity can become comparable to the local sound speed. This raises a validity issue regarding the assumption of local thermodynamic equilibrium.

Physically, equilibrium is maintained only if the collisional relaxation timescale, $t_r \sim (\rho c_s \sigma)^{-1}$, is significantly shorter than the dynamical timescale of the bulk motion, characterized by the shell crossing time $t_{\text{sc}} \sim \Delta R/U$. At radii $R \sim 10^{-1}R_s$, the combination of low density and high bulk velocity results in these two timescales becoming comparable ($t_r \sim t_{\text{sc}}$). In reality, if the expansion speed is too high, the collision rate becomes insufficient to maintain thermal equilibrium or effectively transport heat. Consequently, the outer shells would not gain thermal energy as efficiently as predicted by equilibrium theory, and the expansion would naturally be self-regulated and suppressed. This mechanism prevents the system from entering an unphysical regime where thermally driven expansion exceeds the sound speed. However, in our standard hydrodynamical framework, thermal equilibrium is enforcing instantaneously via the equation of state (Eq. (23)), which lacks the intrinsic physical mechanism to dampen the expansion when the collision rate is insufficient. While a rigorous treatment requires solving the full collisional Boltzmann equation [see e.g., 128], we adopt a simplified approach here. We introduce a phenomenological pressure modification factor, f_p , to account for this non-equilibrium effect. This factor reduces the effective pressure when the relaxation timescale becomes significant:

$$f_p = \left(\frac{t_r}{t_{\text{sc}}} + 1 \right)^{-1}. \quad (\text{A13})$$

[1] X. Fan *et al.* (SDSS), *Astron. J.* **122**, 2833 (2001), arXiv:astro-ph/0108063.

[2] C. J. Willott, R. J. McLure, and M. J. Jarvis, *Astrophys. J. Lett.* **587**, L15 (2003), arXiv:astro-ph/0303062.

[3] X. Fan, E. Banados, and R. A. Simcoe, *Ann. Rev. Astron. Astrophys.* **61**, 373 (2023), arXiv:2212.06907 [astro-ph.GA].

[4] A. Heger, C. L. Fryer, S. E. Woosley, N. Langer, and D. H. Hartmann, *Astrophys. J.* **591**, 288 (2003), arXiv:astro-ph/0212469.

[5] E. E. Salpeter, *Astrophys. J.* **140**, 796 (1964).

[6] P. F. Hopkins and E. Quataert, *Mon. Not. Roy. Astron. Soc.* **407**, 1529 (2010), arXiv:0912.3257 [astro-ph.CO].

[7] K. Inayoshi, E. Visbal, and Z. Haiman, *Ann. Rev. Astron. Astrophys.* **58**, 27 (2020), arXiv:1911.05791 [astro-ph.GA].

[8] G. Kauffmann and M. Haehnelt, *Mon. Not. Roy. Astron. Soc.* **311**, 576 (2000), arXiv:astro-ph/9906493.

[9] A. K. Bhowmick *et al.*, *Mon. Not. Roy. Astron. Soc.* **533**, 1907 (2024), arXiv:2406.14658 [astro-ph.GA].

[10] J. P. Gardner *et al.*, *Space Sci. Rev.* **123**, 485 (2006), arXiv:astro-ph/0606175.

[11] J. Matthee *et al.*, *Astrophys. J.* **963**, 129 (2024), arXiv:2306.05448 [astro-ph.GA].

[12] J. E. Greene *et al.*, *Astrophys. J.* **964**, 39 (2024).

[13] I. Labbe *et al.*, *Astrophys. J.* **978**, 92 (2025), arXiv:2306.07320 [astro-ph.GA].

[14] K. Inayoshi, *Astrophys. J. Lett.* **988**, L22 (2025).

[15] V. Kokorev *et al.*, *Astrophys. J.* **968**, 38 (2024), arXiv:2401.09981 [astro-ph.GA].

[16] D. D. Kocevski *et al.*, arXiv e-prints , arXiv:2404.03576 (2024), arXiv:2404.03576 [astro-ph.GA].

[17] A. D. Goulding *et al.*, *Astrophys. J. Lett.* **955**, L24 (2023), arXiv:2308.02750 [astro-ph.GA].

[18] R. Maiolino *et al.*, *Astron. Astrophys.* **691**, A145 (2024), arXiv:2308.01230 [astro-ph.GA].

[19] C.-H. Chen, L. C. Ho, R. Li, and M.-Y. Zhuang, *Astrophys. J.* **983**, 60 (2025).

[20] A. Bogdan *et al.*, *Nature Astron.* **8**, 126 (2024), arXiv:2305.15458 [astro-ph.GA].

[21] M. Volonteri, *Astron. Astrophys. Rev.* **18**, 279 (2010), arXiv:1003.4404 [astro-ph.CO].

[22] L. Barack *et al.*, *Class. Quant. Grav.* **36**, 143001 (2019), arXiv:1806.05195 [gr-qc].

[23] T. Chantavat, S. Chongchitnan, and J. Silk, *Mon. Not. Roy. Astron. Soc.* **522**, 3256 (2023), arXiv:2302.09763 [astro-ph.SR].

[24] V. Bromm and A. Loeb, *Astrophys. J.* **596**, 34 (2003), arXiv:astro-ph/0212400.

[25] M. C. Begelman, M. Volonteri, and M. J. Rees, *Mon. Not.*

Roy. Astron. Soc. **370**, 289 (2006), arXiv:astro-ph/0602363.

[26] G. Lodato and P. Natarajan, *Mon. Not. Roy. Astron. Soc.* **371**, 1813 (2006), arXiv:astro-ph/0606159.

[27] C. Shang, G. Bryan, and Z. Haiman, *Mon. Not. Roy. Astron. Soc.* **402**, 1249 (2010), arXiv:0906.4773 [astro-ph.CO].

[28] M. A. Latif, D. R. G. Schleicher, W. Schmidt, and J. Niemeyer, *Mon. Not. Roy. Astron. Soc.* **433**, 1607 (2013), arXiv:1304.0962 [astro-ph.CO].

[29] S. C. O. Glover and P. W. J. L. Brand, *Mon. Not. Roy. Astron. Soc.* **321**, 385 (2001), arXiv:astro-ph/0005576.

[30] B. Devecchi, M. Volonteri, E. M. Rossi, M. Colpi, and S. Portegies Zwart, *Mon. Not. Roy. Astron. Soc.* **421**, 1465 (2012), arXiv:1201.3761 [astro-ph.CO].

[31] K. Kritos, E. Berti, and J. Silk, *Mon. Not. Roy. Astron. Soc.* **531**, 133 (2024), arXiv:2404.11676 [astro-ph.HE].

[32] M. A. Latif and A. Ferrara, *Publ. Astron. Soc. Austral.* **33**, e051 (2016), arXiv:1605.07391 [astro-ph.GA].

[33] M. G. Roberts *et al.*, *JCAP* **01**, 060 (2025), arXiv:2410.17480 [astro-ph.GA].

[34] F. Santoro and J. M. Shull, *Astrophys. J.* **643**, 26 (2006), arXiv:astro-ph/0509101.

[35] K. Inayoshi, Z. Haiman, and J. P. Ostriker, *Mon. Not. Roy. Astron. Soc.* **459**, 3738 (2016), arXiv:1511.02116 [astro-ph.HE].

[36] J. L. Johnson, D. J. Whalen, H. Li, and D. E. Holz, *Astrophys. J.* **771**, 116 (2013), arXiv:1211.0548 [astro-ph.CO].

[37] Y. Shi, K. Kremer, M. Y. Grudić, H. J. Gerling-Dunsmore, and P. F. Hopkins, *Mon. Not. Roy. Astron. Soc.* **518**, 3606 (2022), arXiv:2208.05025 [astro-ph.GA].

[38] Z. Haiman, *Astrophys. J.* **613**, 36 (2004), arXiv:astro-ph/0404196.

[39] J. Yoo and J. Miralda-Escude, *Astrophys. J. Lett.* **614**, L25 (2004), arXiv:astro-ph/0406217.

[40] M. Y. Khlopov, *Res. Astron. Astrophys.* **10**, 495 (2010), arXiv:0801.0116 [astro-ph].

[41] A. Escrivà, *Universe* **8**, 66 (2022), arXiv:2111.12693 [gr-qc].

[42] A. Escrivà, F. Kuhnel, and Y. Tada, (2022), 10.1016/B978-0-32-395636-9.00012-8, arXiv:2211.05767 [astro-ph.CO].

[43] Y. B. Zel'dovich and I. D. Novikov, *Sov. Astron.* **10**, 602 (1967).

[44] S. Hawking, *Mon. Not. Roy. Astron. Soc.* **152**, 75 (1971).

[45] B. J. Carr and S. W. Hawking, *Mon. Not. Roy. Astron. Soc.* **168**, 399 (1974).

[46] B. Carr and J. Silk, *Mon. Not. Roy. Astron. Soc.* **478**, 3756 (2018), arXiv:1801.00672 [astro-ph.CO].

[47] K. Inomata, M. Kawasaki, and Y. Tada, *Phys. Rev. D* **94**, 043527 (2016), arXiv:1605.04646 [astro-ph.CO].

[48] K. C. Freeman, *Astrophys. J.* **160**, 811 (1970).

[49] T. G. Brainerd, R. D. Blandford, and I. Smail, *Astrophys. J.* **466**, 623 (1996), arXiv:astro-ph/9503073.

[50] E. Komatsu *et al.* (WMAP), *Astrophys. J. Suppl.* **192**, 18 (2011), arXiv:1001.4538 [astro-ph.CO].

[51] N. Aghanim *et al.* (Planck), *Astron. Astrophys.* **641**, A6 (2020), [Erratum: *Astron. Astrophys.* 652, C4 (2021)], arXiv:1807.06209 [astro-ph.CO].

[52] P. J. E. Peebles, *The large-scale structure of the universe* (1980).

[53] M. Davis, G. Efstathiou, C. S. Frenk, and S. D. M. White, *Astrophys. J.* **292**, 371 (1985).

[54] H. Mo, F. C. van den Bosch, and S. White, *Galaxy Formation and Evolution* (2010).

[55] M. Vogelsberger, F. Marinacci, P. Torrey, and E. Puchwein, *Nature Rev. Phys.* **2**, 42 (2020), arXiv:1909.07976 [astro-ph.GA].

[56] D. Lynden-Bell, *Mon. Not. Roy. Astron. Soc.* **136**, 101 (1967).

[57] C. R. Argüelles, M. I. Díaz, A. Krut, and R. Yunis, *Mon. Not. Roy. Astron. Soc.* **502**, 4227 (2021), arXiv:2012.11709 [astro-ph.GA].

[58] M. Cirelli, A. Strumia, and J. Zupan, (2024), arXiv:2406.01705 [hep-ph].

[59] J. S. Bullock and M. Boylan-Kolchin, *Ann. Rev. Astron. Astrophys.* **55**, 343 (2017), arXiv:1707.04256 [astro-ph.CO].

[60] L. V. Sales, A. Wetzel, and A. Fattah, *Nature Astronomy* **6**, 897 (2022), arXiv:2206.05295 [astro-ph.GA].

[61] D. N. Spergel and P. J. Steinhardt, *Phys. Rev. Lett.* **84**, 3760 (2000), arXiv:astro-ph/9909386.

[62] S. Tulin and H.-B. Yu, *Phys. Rept.* **730**, 1 (2018), arXiv:1705.02358 [hep-ph].

[63] C. A. Correa, *Mon. Not. Roy. Astron. Soc.* **503**, 920 (2021), arXiv:2007.02958 [astro-ph.GA].

[64] M. Vogelsberger, J. Zavala, and A. Loeb, *Mon. Not. Roy. Astron. Soc.* **423**, 3740 (2012), arXiv:1201.5892 [astro-ph.CO].

[65] M. Rocha, A. H. G. Peter, J. S. Bullock, M. Kaplinghat, S. Garrison-Kimmel, J. Onorbe, and L. A. Moustakas, *Mon. Not. Roy. Astron. Soc.* **430**, 81 (2013), arXiv:1208.3025 [astro-ph.CO].

[66] A. H. G. Peter, M. Rocha, J. S. Bullock, and M. Kaplinghat, *Mon. Not. Roy. Astron. Soc.* **430**, 105 (2013), arXiv:1208.3026 [astro-ph.CO].

[67] J. Zavala, M. Vogelsberger, and M. G. Walker, *Mon. Not. Roy. Astron. Soc.* **431**, L20 (2013), arXiv:1211.6426 [astro-ph.CO].

[68] K. A. Oman *et al.*, *Mon. Not. Roy. Astron. Soc.* **452**, 3650 (2015), arXiv:1504.01437 [astro-ph.GA].

[69] D. Yang and H.-B. Yu, *Phys. Rev. D* **104**, 103031 (2021), arXiv:2102.02375 [astro-ph.GA].

[70] D. Gilman, J. Bovy, T. Treu, A. Nierenberg, S. Birrer, A. Benson, and O. Sameie, *Mon. Not. Roy. Astron. Soc.* **507**, 2432 (2021), arXiv:2105.05259 [astro-ph.CO].

[71] S. Adhikari *et al.*, (2022), arXiv:2207.10638 [astro-ph.CO].

[72] S. Balberg, S. L. Shapiro, and S. Inagaki, *Astrophys. J.* **568**, 475 (2002), arXiv:astro-ph/0110561.

[73] S. Balberg and S. L. Shapiro, *Phys. Rev. Lett.* **88**, 101301 (2002), arXiv:astro-ph/0111176.

[74] F. Jiang, Z. Jia, H. Zheng, L. C. Ho, K. Inayoshi, X. Shen, M. Vogelsberger, and W.-X. Feng, (2025), arXiv:2503.23710 [astro-ph.GA].

[75] C. R. Argüelles, K. Boshkayev, A. Krut, G. Nurbakhyt, J. A. Rueda, R. Ruffini, J. D. Uribe-Suárez, and R. Yunis, *Mon. Not. Roy. Astron. Soc.* **523**, 2209 (2023), arXiv:2305.02430 [astro-ph.CO].

[76] A. P. Lightman and S. L. Shapiro, *Rev. Mod. Phys.* **50**, 437 (1978).

[77] D. Lynden-Bell and P. P. Eggleton, *Mon. Not. Roy. Astron. Soc.* **191**, 483 (1980).

[78] W.-X. Feng, H.-B. Yu, and Y.-M. Zhong, *Astrophys. J. Lett.* **914**, L26 (2021), arXiv:2010.15132 [astro-ph.CO].

[79] Y.-M. Zhong, D. Yang, and H.-B. Yu, *Mon. Not. Roy. Astron. Soc.* **526**, 758 (2023), arXiv:2306.08028 [astro-ph.CO].

[80] J. Pollack, D. N. Spergel, and P. J. Steinhardt, *Astrophys. J.* **804**, 131 (2015), arXiv:1501.00017 [astro-ph.CO].

[81] R. Essig, S. D. McDermott, H.-B. Yu, and Y.-M. Zhong, *Phys. Rev. Lett.* **123**, 121102 (2019), arXiv:1809.01144 [hep-ph].

[82] J. Choquette, J. M. Cline, and J. M. Cornell, *JCAP* **07**, 036 (2019), arXiv:1812.05088 [astro-ph.CO].

[83] X. Shen, P. F. Hopkins, L. Necib, F. Jiang, M. Boylan-Kolchin, and A. Wetzel, *Mon. Not. Roy. Astron. Soc.* **506**, 4421 (2021), arXiv:2102.09580 [astro-ph.GA].

[84] H. Xiao, X. Shen, P. F. Hopkins, and K. M. Zurek, *JCAP* **07**,

039 (2021), arXiv:2103.13407 [astro-ph.CO].

[85] T. Shen, X. Shen, H. Xiao, M. Vogelsberger, and F. Jiang, (2025), arXiv:2504.00075 [astro-ph.GA].

[86] N. J. Outmezguine, K. K. Boddy, S. Gad-Nasr, M. Kaplinghat, and L. Sagunski, *Mon. Not. Roy. Astron. Soc.* **523**, 4786 (2023), arXiv:2204.06568 [astro-ph.GA].

[87] S. Yang, X. Du, Z. C. Zeng, A. Benson, F. Jiang, E. O. Nadler, and A. H. G. Peter, *Astrophys. J.* **946**, 47 (2023), arXiv:2205.02957 [astro-ph.CO].

[88] S. Gad-Nasr, K. K. Boddy, M. Kaplinghat, N. J. Outmezguine, and L. Sagunski, *JCAP* **05**, 131 (2024), arXiv:2312.09296 [astro-ph.GA].

[89] J. Koda and P. R. Shapiro, *Mon. Not. Roy. Astron. Soc.* **415**, 1125 (2011), arXiv:1101.3097 [astro-ph.CO].

[90] O. Sameie, P. Creasey, H.-B. Yu, L. V. Sales, M. Vogelsberger, and J. Zavala, *Mon. Not. Roy. Astron. Soc.* **479**, 359 (2018), arXiv:1801.09682 [astro-ph.GA].

[91] A. Robertson, D. Harvey, R. Massey, V. Eke, I. G. McCarthy, M. Jauzac, B. Li, and J. Schaye, *Mon. Not. Roy. Astron. Soc.* **488**, 3646 (2019), arXiv:1810.05649 [astro-ph.CO].

[92] A. Banerjee, S. Adhikari, N. Dalal, S. More, and A. Kravtsov, *JCAP* **02**, 024 (2020), arXiv:1906.12026 [astro-ph.CO].

[93] V. M. Sabarish, M. Brüggen, K. Schmidt-Hoberg, and M. S. Fischer, *Astron. Astrophys.* **703**, A142 (2025), arXiv:2505.14779 [astro-ph.CO].

[94] I. Palubski, O. Sloane, M. Kaplinghat, M. Lisanti, and F. Jiang, *JCAP* **09**, 074 (2024), arXiv:2402.12452 [astro-ph.CO].

[95] M. S. Fischer, K. Dolag, and H.-B. Yu, *Astron. Astrophys.* **689**, A300 (2024), arXiv:2403.00739 [astro-ph.CO].

[96] R. Penrose, *Phys. Rev. Lett.* **14**, 57 (1965).

[97] S. W. Hawking, *Commun. Math. Phys.* **25**, 152 (1972).

[98] W.-X. Feng, H.-B. Yu, and Y.-M. Zhong, *JCAP* **05**, 036 (2022), arXiv:2108.11967 [astro-ph.CO].

[99] W.-X. Feng, H.-B. Yu, and Y.-M. Zhong, (2025), arXiv:2506.17641 [astro-ph.GA].

[100] S. L. Shapiro and V. Paschalidis, *Phys. Rev. D* **89**, 023506 (2014), arXiv:1402.0005 [astro-ph.CO].

[101] S. L. Shapiro, *Phys. Rev. D* **98**, 023021 (2018), arXiv:1809.02618 [astro-ph.HE].

[102] J. R. Oppenheimer and H. Snyder, *Phys. Rev.* **56**, 455 (1939).

[103] C. W. Misner and D. H. Sharp, *Phys. Rev.* **136**, B571 (1964).

[104] M. M. May and R. H. White, *Phys. Rev.* **141**, 1232 (1966).

[105] K. A. van Riper, *Astrophys. J.* **221**, 304 (1978).

[106] K. A. van Riper, *Astrophys. J.* **232**, 558 (1979).

[107] T. W. Baumgarte, S. L. Shapiro, and S. A. Teukolsky, *Astrophys. J.* **443**, 717 (1995).

[108] S. Chapman and T. G. Cowling, *The mathematical theory of non-uniform gases. an account of the kinetic theory of viscosity, thermal conduction and diffusion in gases* (1970).

[109] C. Eckart, *Phys. Rev.* **58**, 919 (1940).

[110] C. W. Misner, K. S. Thorne, and J. A. Wheeler, *Gravitation* (W. H. Freeman, San Francisco, 1973).

[111] M. Liebendoerfer, A. Mezzacappa, and F.-K. Thielemann, *Phys. Rev. D* **63**, 104003 (2001), arXiv:astro-ph/0012201.

[112] R. C. Tolman, *Phys. Rev.* **55**, 364 (1939).

[113] J. R. Oppenheimer and G. M. Volkoff, *Phys. Rev.* **55**, 374 (1939).

[114] W. C. Hernandez and C. W. Misner, *Astrophys. J.* **143**, 452 (1966).

[115] S. W. Hawking and G. F. R. Ellis, *The Large Scale Structure of Space-Time*, Cambridge Monographs on Mathematical Physics (Cambridge University Press, 2023).

[116] J. F. Navarro, C. S. Frenk, and S. D. M. White, *Astrophys. J.* **462**, 563 (1996), arXiv:astro-ph/9508025.

[117] J. F. Navarro, C. S. Frenk, and S. D. M. White, *Astrophys. J.* **490**, 493 (1997), arXiv:astro-ph/9611107.

[118] H. Nishikawa, K. K. Boddy, and M. Kaplinghat, *Phys. Rev. D* **101**, 063009 (2020), arXiv:1901.00499 [astro-ph.GA].

[119] K.-J. Ahn and P. R. Shapiro, *Mon. Not. Roy. Astron. Soc.* **363**, 1092 (2005), arXiv:astro-ph/0412169.

[120] W. J. G. de Blok, *Adv. Astron.* **2010**, 789293 (2010), arXiv:0910.3538 [astro-ph.CO].

[121] A. Di Cintio, M. Tremmel, F. Governato, A. Pontzen, J. Zavala, A. Bastidas Fry, A. Brooks, and M. Vogelsberger, *Mon. Not. Roy. Astron. Soc.* **469**, 2845 (2017), arXiv:1701.04410 [astro-ph.GA].

[122] M. Kaplinghat, T. Ren, and H.-B. Yu, *JCAP* **06**, 027 (2020), arXiv:1911.00544 [astro-ph.GA].

[123] T. Meshveliani, J. Zavala, and M. R. Lovell, *Phys. Rev. D* **107**, 083010 (2023), arXiv:2210.01817 [astro-ph.GA].

[124] F. C. van den Bosch and S. Dattathri, “Dynamics in the cores of self-interacting dark matter halos: Reduced stalling and accelerated core collapse,” (2025), arXiv:2511.14912 [astro-ph.GA].

[125] H. Bondi, *Mon. Not. Roy. Astron. Soc.* **112**, 195 (1952).

[126] J. Hu, Y. Shen, Y.-Q. Lou, and S. Zhang, *Mon. Not. R. Astron. Soc.* **365**, 345 (2006), arXiv:astro-ph/0510222 [astro-ph].

[127] R. Courant, K. Friedrichs, and H. Lewy, *IBM Journal of Research and Development* **11**, 215 (1967).

[128] J. Gurian and S. May, *Phys. Rev. Lett.* **135**, 221001 (2025), arXiv:2505.15903 [astro-ph.CO].